Low dissipation of earthquake energy along faults that follow pre-existing weaknesses: field and microstructural observations of Malawi's Bilila-Mtakataka Fault

Jack Nicholas Williams[1], Ake Fagereng[1], Luke N J Wedmore[2], Juliet Biggs[3], Hassan Mdala[4], Felix Mphepo[4], and Michael Hodge[1]

[1]Cardiff University
[2]University of Bristol
[3]University of Bristol, UK
[4]Geological Survey of Malawi

November 22, 2022

Abstract

Fracturing and gouge formation absorb [?]50% of earthquake energy on low displacement (<1-2 km) faults in isotropic crust. To assess how these processes absorb earthquake energy in anisotropic crust, we performed field and microstructural investigations on the 110 km long, 0.4-1.2 km displacement, Bilila-Mtakataka Fault (BMF), Malawi. Where the fault is parallel to surface metamorphic fabrics, macroscale fractures define a 5-20 m wide damage zone. This is narrow relative to where the BMF is foliation-oblique (20-80 m), and to faults with comparable displacement in isotropic crust (~40-120 m). There is minimal evidence for cataclasis and microfracturing along the BMF; therefore, despite its 110 km length and geomorphic evidence for M_W 7-8 earthquakes, widespread fault zone fracturing has not occurred. We attribute lack of damage to fault growth along shallow and deep-seated pre-existing weaknesses. This conclusion implies that earthquake energy dissipates differently along incipient faults in isotropic and anisotropic crust.

Low dissipation of earthquake energy along faults that follow pre-existing weaknesses: field and microstructural observations of Malawi's Bilila-Mtakataka Fault

Jack N. Williams[a,b], Åke Fagereng[a], Luke N.J. Wedmore[b], Juliet Biggs[b], Hassan Mdala[c], Felix Mphepo[c], Michael Hodge[a]

Affiliations

[a]*School of Earth and Environmental Sciences, Cardiff University, Cardiff, UK*

[b]*School of Earth Sciences, University of Bristol, Bristol, UK*

[c]*Geological Survey Department, Mzuzu Regional Office, Mzuzu, Malawi*

Abstract

Fracturing and gouge formation absorb ≥50% of earthquake energy on low displacement (<1-2 km) faults in isotropic crust. To assess how these processes absorb earthquake energy in anisotropic crust, we performed field and microstructural investigations on the 110 km long, 0.4-1.2 km displacement, Bilila-Mtakataka Fault (BMF), Malawi. Where the fault is parallel to surface metamorphic fabrics, macroscale fractures define a 5-20 m wide damage zone. This is narrow relative to where the BMF is foliation-oblique (20-80 m), and to faults with comparable displacement in isotropic crust (~40-120 m). There is minimal evidence for cataclasis and microfracturing along the BMF; therefore, despite its 110 km length and geomorphic evidence for M_W 7-8 earthquakes, widespread fault zone fracturing has not occurred. We attribute lack of damage to fault growth along shallow and deep-seated pre-existing weaknesses. This conclusion implies that earthquake energy dissipates differently along incipient faults in isotropic and anisotropic crust.

Key points

- The Bilila-Mtakataka Fault in Malawi has a narrow (5-20 m) footwall damage zone given its 0.4-1.2 km displacement and 110 km length.
- Gouge formation is limited, and the Bilila-Mtakataka Fault has a low maximum displacement to length ratio.
- Limited fracturing implies earthquakes along pre-existing crustal weaknesses dissipate less energy into fault zones than in intact crust.

Plain language summary

Earthquakes release energy, some of which is radiated as seismic energy to the Earth's surface where it causes ground shaking that poses a risk to human life and infrastructure. However, much of this earthquake energy is also dissipated into the rocks surrounding the fault, which causes them to fracture and fragment. This fracturing process is thought to be particularly prevalent in low displacement (≤1-2 km total displacement) faults as the fault grows by breaking surrounding intact rock. In this study, we demonstrate through field and microscale observations of the Bilila-Mtakataka Fault in southern Malawi that despite its low displacement (0.4-1.2 km) and inferred history of M_W 7-8 earthquakes, only limited fracturing of the surrounding rock has occurred. We propose that this limited fracturing results from earthquakes along the Bilila-Mtakataka Fault that rupture along pre-existing weaknesses in Malawi's crust. If true, then the partitioning of earthquake energy between seismic energy and fracturing in the surrounding crust will be influenced by whether the earthquake is exploiting a pre-existing weakness in the Earth's crust.

1. Introduction

Pre-existing mechanical weaknesses in the crust, such as joints, bedding planes, and metamorphic fabrics can profoundly affect earthquake rupture propagation [*Allen*, 2005; *Hecker et al.*, 2021; *Heermance et al.*, 2003; *Litchfield et al.*, 2018]. Over multiple earthquake cycles, these weaknesses may therefore influence the progressive development of fault rocks and wall rock fracturing, and thus the ability of faults to transmit fluids [*Butler et al.*, 2008; *Crider & Peacock*, 2004] and to be detected in geophysical surveys [*Kelly et al.*, 2017]. Furthermore, in continental rifts, normal faults that reactivate well-oriented pre-existing weaknesses can lengthen rapidly at relatively small displacements [*Collanega et al.*, 2019; *Hecker et al.*, 2021; *Paton*, 2006; *Walsh et al.*, 2002]. Interactions between pre-existing crustal weaknesses and faults can therefore affect seismic hazard [*Heermance et al.*, 2003] and the extent to which fault zone fluid flow can focus minerals into economically viable deposits [*Micklethwaite & Cox*, 2004].

Fault zone structure is typically described by: (1) one or more relatively narrow 'fault cores' that comprise fault breccias, cataclasites, and/or gouges, and can include one or more principal slip zones [*Sibson*, 1977], and (2) a surrounding 'damage zone', where fracture density is high relative to the host rocks but shear displacements are small and the original protolith is preserved [*Caine et al.*, 1996]. Gouge formation and damage zone fracturing can occur in response to quasi-static fault tip propagation [*Lockner et al.*, 1991; *Renard et al.*, 2018] and chemical alteration [*Lacroix et al.*, 2015]. In seismogenic faults, gouges and damage zones also develop when energy released during an earthquake is partially absorbed by rocks surrounding the fault, as described by:

$$E_T = (E_G + E_F) + E_R$$

(1)

where E_T is the total earthquake energy release, E_R is radiated seismic energy, and E_G and E_F are the energy required to create a slip surface (fracture energy) and slide along that surface (frictional energy) respectively [*Kanamori & Rivera*, 2006]. E_G and E_F cannot be distinguished based on geological observations of fault zones; however, together these terms can be considered to represent dissipative processes that reduce the E_R available to reach the surface [*Kanamori & Rivera*, 2006; *McKay et al.*, 2021; *Shipton et al.*, 2006].

Several lines of evidence suggest that in isotropic crust, fault damage and gouge primarily form during early fault growth. First, a scaling between damage zone width and total fault displacement is only observed for displacements <1-2 km [*Savage & Brodsky*, 2011; *Torabi et al.*, 2020]. Field observations and particle analysis of gouges also suggest that E_G and E_F account for a much higher proportion of E_T in earthquakes in intact rock (≥50%) than in earthquakes along high displacement faults [1-10%; *Chester et al.*, 2005; *Wilson et al.*, 2005]. Finally, damage zone fracturing is particularly prevalent at geometrical complexities [*Bistacchi et al.*, 2010; *Childs et al.*, 2009; *Tinti et al.*, 2005], and these complexities tend to be smoothed as fault accumulates displacement [*Sagy et al.*, 2007].

The structural evolution of faults in anisotropic crust is, however, unclear, with examples of foliation-parallel faults that are relatively narrow [*Butler et al.*, 2008; *Heermance et al.*, 2003; *McBeck et al.*, 2019; *Wedmore et al.*, 2020; *Zangerl et al.*, 2006] or of comparable width [*Bistacchi et al.*, 2010; *Soden et al.*, 2014; *Wheeler & Karson*, 1989] to a fault with equivalent displacement that cross-cuts foliation or is hosted in isotropic crust. These contrasting observations may reflect variations in confining pressures and temperatures [*McBeck et al.*, 2019; *Soden et al.*, 2014; *Williams et al.*, 2018], relative orientations of the fault, mechanical weakness, and regional principal stresses [*Donath*, 1961; *Fletcher et al.*, 2020; *Misra et al.*, 2015], the composition and spacing of fabrics [*Beacom et al.*, 2001; *Williams et al.*, 2018], and/or the presence of strain-hardening phyllosilicates [*Bistacchi et al.*, 2010; *Faulkner et al.*, 2008] and mechanically isotropic cataclasite [*Kirkpatrick et al.*, 2013]. Therefore, when investigating the structural evolution of faults in anisotropic crust, it is important that the influence of these various factors can be separated.

Here, we investigate the Bilila-Mtakataka Fault (BMF), a 110 km long normal fault in southern Malawi with geomorphic evidence for Late Quaternary M_W 7-8 earthquakes [*Hodge et al.*, 2018, 2020; *Jackson & Blenkinsop*, 1997]. The BMF provides important constraints on near-surface fault zone development in anisotropic crust as it shows variable geometrical relationships with surrounding Proterozoic metamorphic fabrics, and thick sequences of isotropic cataclasite have not developed [*Hodge et al.*, 2018]. Furthermore, in the context of normal fault growth models [*Rotevatn et al.*, 2019; *Walsh et al.*, 2002], the BMF's 0.4-1.2 km maximum displacement implies it is in its early stages of growth, and field examples of active crustal-scale low-displacement normal fault are comparatively rare [*Biegel & Sammis*, 2004; *Gawthorpe & Leeder*, 2000]. Our field and microstructural analyses of the BMF can therefore document the effects of pre-existing anisotropies on earthquake energy dissipation around an incipient but >100 km long normal fault.

2. The Bilila-Mtakataka Fault

The BMF is situated in southern Malawi in the amagmatic Makanjira Graben, which geodetic models indicate accommodates ~0.7 mm/yr extension between the San and Rovuma plates near the southern end of the East African Rift's Western Branch [Fig. 1; *Wedmore et al.*, 2021]. The BMF is expressed at the surface by an escarpment that juxtaposes Proterozoic Southern

Irumide Belt gneisses in the footwall against hanging wall post-Miocene sediments and, at the 1-10 km scale, follows gently to steeply dipping NW-SE striking amphibolite-granulite facies Southern Irumide Belt metamorphic fabrics [Fig. 1b; *Dawson & Kirkpatrick*, 1968; *Hodge et al.*, 2018; *Jackson & Blenkinsop*, 1997; *Laõ-Dávila et al.*, 2015; *Walshaw*, 1965]. At the base of the escarpment is a continuous 110 km long, 5-28 m high soil-mantled scarp, which on the basis of topographic profiles, is interpreted to have formed in at least two M_W 7.8 ± 0.3 earthquakes, with the most recent event likely occurring within the past 10,000 years [*Hodge et al.*, 2018, 2020]. Variations in scarp height and strike have been used to divide the BMF into six sections (Figs. 1a and b); however, at depths >5 km, these sections may root onto one or two sub-planar weaknesses [*Hodge et al.*, 2018].

The BMF footwall escarpment has a maximum height of ~300 m (Fig. 1). Several groundwater boreholes in the BMF hanging wall intersected basement rock at depths <40 m, while others encountered sediments to a maximum drilling depth of 60 m [Fig.1a; *Dawson & Kirkpatrick*, 1968; *Walshaw*, 1965]. Locally, hanging wall basement rock is exposed adjacent to the BMF scarp [*Walshaw*, 1965]. These observations suggest a relatively thin but variable-thickness sequence of post-Miocene sediments in the BMF hanging wall. A conservative upper bound for their thickness is 500 m, which is the thickness of syn-rift sediments across strike of the BMF's northern tip at the southwestern end of Lake Malawi (Fig. 1), and where total regional extension is greater than elsewhere along the BMF [*Scholz et al.*, 2020]. Combining a range of hanging wall sediment thicknesses of 50-500 m with the 300 m high footwall escarpment and an estimated BMF dip of 42-60° [*Hodge et al.*, 2018; *Stevens et al.*, 2021], we propose its maximum displacement, D_{max}, is 0.4-1.2 km. Given a fault length (L) of 110 km, the D_{max}:L ratio is ~0.004-0.011. In the context of normal fault growth models, these observations place the BMF in the initial stages of growth (20-30% of fault lifespan) with substantial fault lengthening but relatively little displacement [*Rotevatn et al.*, 2019; *Walsh et al.*, 2002].

3. Field and Microstructural Observations

Samples and structural measurements were collected along two rivers oriented approximately perpendicular to the BMF scarp near the villages of Kasinje and Mua (Figs. 1-3, Table S1). These sites were chosen because they represent locations with fault-parallel and fault-oblique foliations. Microstructural investigations were made with a petrological microscope on thin sections cut perpendicular to a foliation where present. To quantify fracture density in these samples, we measured the length of microfractures in quartz and feldspar grains in three 8-15 mm^2 regions per sample using FracPaQ v2.2 [*Healy et al.*, 2017], and then divided the total microfracture length by the region's quartzofeldspathic grain area [*Wedmore et al.*, 2020]. Backscatter electron imaging and Energy Dispersive Spectroscopy (EDS) analyses were also performed on selected samples (Table S1) using a Zeiss Sigma HD Field Emission Gun Analytical Scanning Electron Microscope (SEM) in the School of Earth and Environmental Sciences at Cardiff University. Samples were coated with 10 nm of carbon, and the SEM data were acquired with a 15 keV beam energy, 8.9 mm working distance, and 60 μm and 120 μm aperture for point analyses or EDS maps respectively.

Along the ~ 20 km long Mua segment, the BMF scarp is oblique to a gently-dipping curvi-planar cohesive foliation in biotite gneisses (Fig. 2a). This gneissic foliation is defined by mm-spaced bands of quartz + feldspar alternating with bands of biotite + garnet + hornblende (Fig. S2d). Samples from within 2 m of the 13 m high BMF scarp by the Naminkikowe River, including directly from the scarp itself, contain mm-scale quartzofeldspathic and biotite grains that are locally (15-30% by area) surrounded by a fine-grained (<10 μm grain size) matrix that consists of fragmented quartzofeldspathic and chlorite grains (Figs. 2, S2, and S3).

At distances 2-20 m from the scarp, a gently NE-dipping set of joints, with a subordinate subvertical N-S striking joint set, is observed in outcrop (Fig. 2c). Joint spacing is 0.01-0.1 m near the fault and increases to >0.1 m at distances 20-350 m from the scarp (Figs. 2c and S2c). In all samples 2-350 m from the BMF scarp at Mua, mm-scale quartzofeldspathic grains are crosscut by a microfractures, however, there is no evidence for shear across these microfractures. Microfractures are 1-50 μm thick and contain a brown fine-grained fill identified by qualitative EDS as chlorite and Fe-oxide (Figs. S2 and S4). Microfracture density (~1-4 mm^{-1}) does not increase with proximity to the fault over our 350 m long transect (Figs. 4 and S2).

Along the ~20-km long Kasinje segment, the BMF is parallel to a foliation defined by quartzofeldspathic bands alternating with bands of hornblende + garnet + biotite (Fig. 3). Adjacent to the 16 m high BMF scarp by the Mtuta River, including in scattered exposure on its immediate hanging wall side, is a 5 m wide interval of fractured rock with 0.1-1 m spaced, foliation-parallel joints (Figs. 3b and S5a). In this macroscopically fractured interval, bands of intact quartzofeldspathic domains and calcite veins are locally interlayered with 10 – 100 μm bands of fragmented plagioclase and calcite (Figs. 3d, S4d, S5b). No macroscopic, fault-related deformation is observed in the hanging wall more than 16 m from the scarp (Figs. 3a and S4f). Samples from this hanging wall section and >5 m into the footwall contain mm-scale quartzofeldspathic grains that are cross-cut by chlorite veins (Figs. S4 and S5). As in the Mua transect, microscale fracture density is 1-4 mm^{-1} and does not vary systematically along the 80 m long transect (Fig. 4).

4. Bilila-Mtakataka Fault Zone Structure

We now place our field and microstructural observations of the BMF in the context of conceptual fault zone structure models [*Caine et al.*, 1996]. At Mua, we interpret that the fine-grained matrix observed in a 2 m thick cohesive unit adjacent to the scarp (Figs. 2 and S3) formed from grain-scale fragmentation and sliding (i.e., comminution) during slip along the BMF. Evidence for displacement along the BMF is localised within this protocataclasite unit [*sensu Woodcock & Mort*, 2008]. This 2 m wide unit provides a minimum estimate of fault core width at Mua, because the hanging wall is not exposed at this locality (Figs. 2a and 4). We define the BMF footwall damage zone at Mua as the region 2-20 m from the scarp where there is no evidence of grain-scale comminution but relatively closely spaced (0.01-0.1 m) joints are present (Fig. 2c). Although the hanging wall damage zone is not exposed at Mua, it is unlikely to be more than three times wider than the 20 m footwall damage zone [*Biegel & Sammis*, 2004; *Savage & Brodsky*, 2011]. Therefore, we suggest that the total width of the damage zone at Mua is 20-80 m.

A near complete footwall to hanging wall section through the BMF is exposed at Kasinje (Fig. 3), however, no distinct gouge or cataclasite layers that would typically define a fault core are observed. We cannot rule out that the lack of a fault core represents incomplete exposure or sampling, although a 2 m thick protocataclasite similar to that observed at Mua should have been clearly visible. We interpret that the full width of the BMF damage zone is contained within the interval of closely spaced foliation-parallel joints that extends ~5 m from the scarp into the footwall, < 16 m into the hanging wall (Fig. 3a) and are not seen outside this interval.

Calcite veins are observed within the damage zone at Kasinje. Calcite is a common alteration product in fault zones elsewhere in Malawi [*Williams et al.*, 2019], and these veins may be linked to precipitation from shallow (depths <5 km) Ca^{2+} rich meteoric waters in Malawi [*Dávalos-Elizondo et al.*, 2021]. Veins at Mua and >5 m from the scarp at Kasinje are dominantly made of Fe-oxide and chlorite; however, the number of these veins is not related to distance to the BMF scarp (Figs. 4, S2, S4, and S5). These minerals are not a common low temperature (<300 °C) alteration product [*Tulloch*, 1979], nor is dissolved iron typical of hydrothermal fluids in Malawi [*Dávalos-Elizondo et al.*, 2021]. We therefore suggest these veins formed before current rift-related faulting.

Analyses of fault zones are always limited by erosion of incohesive fault rocks and lack of exposure [*Shipton et al.*, 2019]. Nevertheless, at Kasinje the BMF exhibits a composite scarp indicating relatively minor scarp erosion since the most recent BMF earthquake [*Hodge et al.*, 2020]. We also note that incohesive fault rocks are preserved adjacent to fault scarps in similar environments and rock types elsewhere in southern Malawi [*Wedmore et al.*, 2020; *Williams et al.*, 2019] and in other subtropical regions of the East African Rift's Western Branch [*Delvaux et al.*, 2012; *Ring*, 1994; *Vittori et al.*, 1997; *Wheeler & Karson*, 1989].

5. Discussion

5.1 Fault damage and the earthquake energy budget

At both Kasinje and Mua, a macroscopic damage zone is observed. Although there is scatter in data compilations, the ratio between fault displacement and damage zone width is typically ~0.1 for faults with comparable displacement (~10^2-10^3 m) to the BMF [*Savage & Brodsky*, 2011; *Torabi & Berg*, 2011]. The 5-20 m wide damage zone at Kasinje, where the BMF is foliation-parallel, is therefore narrow compared to that predicted for a fault with the same displacement in isotropic crust (40-120 m) and to Mua (20-80 m) where the BMF is foliation-oblique. It follows that when an earthquake on the BMF reactivates near-surface metamorphic foliations, less earthquake energy is dissipated on gouge formation and damage-zone widening (i.e., E_G and E_f in Eq. 1) than if it were propagating through intact rock or across pre-existing weaknesses [*Chester et al.*, 2005; *Heermance et al.*, 2003; *Wilson et al.*, 2005]. Deep-seated (>5 km depth) pre-existing weaknesses may control the BMF's geometry [*Hodge et al.*, 2018; *Williams et al.*, 2019], and so could also contribute to the small release of E_G and E_f during BMF earthquakes. This could account for the lack of increased microfracturing in both the Kasinje and Mua damage zones (Figure 4) compared to the damage zone of a low displacement fault in isotropic crust [*Anders & Wiltschko*, 1994; *Mitchell & Faulkner*, 2009].

If less earthquake energy is spent on dissipative processes during earthquake ruptures on the BMF, these ruptures can radiate more seismic energy and host more coseismic slip [*Heermance et al.*, 2003; *Kanamori & Rivera*, 2006]. This is consistent with relatively large single-event slip/length ratios derived from topographic profiles across the BMF's scarp [*Hodge et al.*, 2020]. Our hypothesis is also supported by studies of continental plate boundary faults, which tend to inherit pre-existing weaknesses and exhibit narrow fault cores relative to their displacement [*McKay et al.*, 2021].

5.2 Implications for fault growth and fault detection in anisotropic crust

Not all faults that follow pre-existing weaknesses exhibit narrow damage zones given their displacement. We suggest that the factors that have facilitated limited wall rock fracturing around the BMF are the favorable orientation of pre-existing weaknesses relative to the regional stresses [Fig. 1a; *Hodge et al.*, 2018; *Williams et al.*, 2019], and that it has yet to develop thick sequences of mechanically isotropic fault cataclasite and gouges [*Kirkpatrick et al.*, 2013]. The relatively low phyllosilicate content and cohesive nature of the foliation around the BMF [*Hodge et al.*, 2018; *Walshaw*, 1965], which prevents multiple foliation planes from reactivating, may also have been important in reducing near-surface fault damage [*Bistacchi et al.*, 2010].

It is common to use geophysical techniques such as seismic refection surveys or fault zone guided waves to investigate the internal structure, mechanics, and extent of active faults [e.g. *Ben-Zion*, 1998; *Cochran et al.*, 2009; *Ellsworth & Malin*, 2011; *Li et al.*, 2014]. However, our study of the BMF implies that it may be challenging to image faults in anisotropic crust using these techniques as it will be difficult to distinguish whether seismic velocity contrasts are caused by the limited fault-related fracturing or the pre-existing weakness itself [*Gulley et al.*, 2017; *Kelly et al.*, 2017; *Simpson et al.*, 2020]. In continental rifts that are accumulating synrift sediments, normal faults that reactivate pre-existing weaknesses can be imaged using seismic reflection surveys [*Collanega et al.*, 2019; *Phillips et al.*, 2016; *Walsh et al.*, 2002]. In these cases, pre-existing weaknesses have been proposed to facilitate rapid fault normal lengthening; however, these studies cannot resolve fault structure at scales <10 m. Our findings from the BMF suggest that normal faults with low displacement to length ratios can form relatively narrow damage zones, even when their length is sufficient to crosscut the crust. During their early stages of growth, these faults will therefore be less effective conduits for fluid flow than a fault with equivalent displacement in isotropic rock.

6. Conclusions

Using field and microstructural observations, we find that where southern Malawi's Bilila-Mtakataka Fault (BMF) is parallel to surrounding metamorphic foliations, it has a relatively narrow damage zone (5-20 m wide), compared to sites where it is foliation-oblique (20-80 m), and to a fault in isotropic crust with comparable displacement [~40-120 m wide for 0.4-1.2 km displacement fault; *Savage & Brodsky*, 2011; *Torabi & Berg*, 2011]. Minimal evidence for BMF microfracturing and grain comminution is observed regardless of whether the BMF is parallel or oblique to surface foliations.

The general observation of poorly developed fault rocks and a narrow damage zone along the BMF, which is particularly clear where it is parallel to surface fabrics, can be explained if earthquake slip on the BMF reactivates pre-existing weaknesses. These weaknesses are favorably oriented in the regional stress state [*Hodge et al.*, 2018; *Williams et al.*, 2019], and we propose reactivation would result in relative little energy being dissipated into accumulating fault gouge and damage [*Kanamori & Rivera*, 2006; *Wilson et al.*, 2005]. This reduction in the amount of dissipative energy is consistent with the high single-event displacement to length ratio of the BMF [*Hodge et al.*, 2020]. We suggest that these observations may be applicable to other low-displacement faults that inherit well-oriented pre-existing weaknesses, particularly normal faults in continental rifts. If true, then since less energy is consumed by dissipative processes on these faults, the seismic energy radiated by earthquakes along them will be unusually large.

Acknowledgements

This work is supported by the EPSRC-Global Challenges Research Fund PREPARE (EP/P028233/1) and SAFER-PREPARED (part of the 'Innovative data services for aquaculture, seismic resilience and drought adaptation in East Africa' grant; EP/T015462/1) projects. TanDEM-X data were provided through DLR proposal DEM_GEOL0686. Figs. 2c and 3b were provided by Johann Diener. All field data is available via Strabospot https://strabospot.org/search?c=MzkxNzUxNy42MjY5NTcxODU2eC0xNzgzMDY1LjE1MzE5MzkxMjd4Ny45OTMzMzMzMzMzMzMzMzMzMzI= (data last accessed 02/19/2020). We thank Antony Oldroyd and Duncan Muir for assistance with making thin sections and technical assistance with the Scanning Electron Microscope respectively.

References

Allen, J. L. (2005). A multi-kilometer pseudotachylyte system as an exhumed record of earthquake rupture geometry at hypocentral depths (Colorado, USA). *Tectonophysics*, *402*(1-4 SPEC. ISS), 37–54. https://doi.org/10.1016/j.tecto.2004.10.017

Anders, M. H., & Wiltschko, D. V. (1994). Microfracturing, paleostress and the growth of faults. *Journal of Structural Geology*, *16*(6), 795–815. https://doi.org/10.1016/0191-8141(94)90146-5

Beacom, L. E., Holdsworth, R. E., McCaffrey, K. J. W., & Anderson, T. B. (2001). A quantitative study of the influence of pre-existing compositional and fabric heterogeneities upon fracture-zone development during basement reactivation. *Geological Society Special Publication*, *186*, 195–211. https://doi.org/10.1144/GSL.SP.2001.186.01.12

Ben-Zion, Y. (1998). Properties of seismic fault zone waves and their utility for imaging low-velocity structures. *Journal of Geophysical Research: Solid Earth*, *103*(6), 12567–12585. https://doi.org/10.1029/98jb00768

Biegel, R. L., & Sammis, C. G. (2004). Relating Fault Mechanics to Fault Zone Structure. *Advances in Geophysics*, *47*(C), 65–111. https://doi.org/10.1016/S0065-2687(04)47002-2

Bistacchi, A., Massironi, M., & Menegon, L. (2010). Three-dimensional characterization of a crustal-scale fault zone: The Pusteria and Sprechenstein fault system (Eastern Alps).

Journal of Structural Geology, *32*(12), 2022–2041. https://doi.org/10.1016/j.jsg.2010.06.003

Butler, R. W. H., Bond, C. E., Shipton, Z. K., Jones, R. R., & Casey, M. (2008). Fabric anisotropy controls faulting in the continental crust. *Journal of the Geological Society*, *165*(2), 449–452. https://doi.org/10.1144/0016-76492007-129

Caine, J. S., Evans, J. P., & Forster, C. B. (1996). Fault zone architecture and permeability structure. *Geology*, *24*(11), 1025–1028.

Chester, J. S., Chester, F. M., & Kronenberg, A. K. (2005). Fracture surface energy of the Punchbowl fault, San Andreas system. *Nature*, *437*(7055), 133–136. https://doi.org/10.1038/nature03942

Childs, C., Manzocchi, T., Walsh, J. J., Bonson, C. G., Nicol, A., & Schöpfer, M. P. J. (2009). A geometric model of fault zone and fault rock thickness variations. *Journal of Structural Geology*, *31*(2), 117–127. https://doi.org/10.1016/j.jsg.2008.08.009

Cochran, E. S., Li, Y. G., Shearer, P. M., Barbot, S., Fialko, Y., & Vidale, J. E. (2009). Seismic and geodetic evidence for extensive, long-lived fault damage zones. *Geology*, *37*(4), 315–318. https://doi.org/10.1130/G25306A.1

Collanega, L., Siuda, K., A.-L. Jackson, C., Bell, R. E., Coleman, A. J., Lenhart, A., et al. (2019). Normal fault growth influenced by basement fabrics: The importance of preferential nucleation from pre-existing structures. *Basin Research*, *31*(4), 659–687. https://doi.org/10.1111/bre.12327

Crider, J. G., & Peacock, D. C. P. (2004). Initiation of brittle faults in the upper crust: A review of field observations. *Journal of Structural Geology*, *26*(4), 691–707. https://doi.org/10.1016/j.jsg.2003.07.007

Dávalos-Elizondo, E., Atekwana, E. A., Atekwana, E. A., Tsokonombwe, G., & Laó-Dávila, D. A. (2021). Medium to low enthalpy geothermal reservoirs estimated from geothermometry and mixing models of hot springs along the Malawi Rift Zone. *Geothermics, 89*. https://doi.org/10.1016/j.geothermics.2020.101963

Dawson, A. L., & Kirkpatrick, I. M. (1968). The geology of the Cape Maclear peninsula and Lower Bwanje valley. *Bulletin of the Geological Survey, Malawi*, *28*.

Delvaux, D., Kervyn, F., Macheyeki, A. S., & Temu, E. B. (2012). Geodynamic significance of the TRM segment in the East African Rift (W-Tanzania): Active tectonics and paleostress in the Ufipa plateau and Rukwa basin. *Journal of Structural Geology, 37,* 161–180. https://doi.org/10.1016/j.jsg.2012.01.008

Donath, F. A. (1961). Experimental study of shear failure in anisotropic rocks. *Geological Society of America Bulletin*, *72*(6), 985–989. https://doi.org/10.1130/0016-7606(1961)72[985:ESOSFI]2.0.CO;2

Ellsworth, W. L., & Malin, P. E. (2011). Deep rock damage in the San Andreas Fault revealed by P- and S-type fault-zone-guided waves. *In Fagereng, A., Toy, V.G., and Rowland, J. (Eds), Geology of the Earthquake Source: A Volume in Honor of Rick Sibson, Geological Society, London, Special Publications.*, *359*(1), 39–53. https://doi.org/10.1144/SP359.3

Faulkner, D. R., Mitchell, T. M., Rutter, E. H., & Cembrano, J. (2008). On the structure and mechanical properties of large strike-slip faults. *Geological Society Special Publication*, *299*(1), 139–150. https://doi.org/10.1144/SP299.9

Fletcher, J. M., Teran, O. J., Rockwell, T. K., Oskin, M. E., Hudnut, K. W., Spelz, R. M., et al. (2020). An analysis of the factors that control fault zone architecture and the importance of fault orientation relative to regional stress. *GSA Bulletin*, 1–21. https://doi.org/10.1130/b35308.1

Gawthorpe, R. L., & Leeder, M. R. (2000). Tectono-sedimentary evolution of active extensional basins. *Basin Research*, *12*(3–4), 195–218. https://doi.org/10.1111/j.1365-

2117.2000.00121.x

Gulley, A. K., Eccles, J. D., Kaipio, J. P., & Malin, P. E. (2017). The effect of gradational velocities and anisotropy on fault-zone trapped waves. *Geophysical Journal International*, *210*(2), 964–978. https://doi.org/10.1093/gji/ggx200

Healy, D., Rizzo, R. E., Cornwell, D. G., Farrell, N. J. C., Watkins, H., Timms, N. E., et al. (2017). FracPaQ: A MATLAB™ toolbox for the quantification of fracture patterns. *Journal of Structural Geology*, *95*, 1–16. https://doi.org/10.1016/j.jsg.2016.12.003

Hecker, S., DeLong, S. B., & Schwartz, D. P. (2021). Rapid strain release on the Bear River fault zone, Utah–Wyoming—The impact of preexisting structure on the rupture behavior of a new normal fault. *Tectonophysics*, *808*(March), 228819. https://doi.org/10.1016/j.tecto.2021.228819

Heermance, R., Shipton, Z. K., & Evans, J. P. (2003). Fault structure control on fault slip and ground motion during the 1999 rupture of the Chelungpu fault, Taiwan. *Bulletin of the Seismological Society of America*, *93*(3), 1034–1050. https://doi.org/10.1785/0120010230

Hodge, M., Fagereng, A., Biggs, J., & Mdala, H. (2018). Controls on Early-Rift Geometry: New Perspectives From the Bilila-Mtakataka Fault, Malawi. *Geophysical Research Letters*, *45*(9), 3896–3905. https://doi.org/10.1029/2018GL077343

Hodge, M., Biggs, J., Fagereng, Mdala, H., Wedmore, L. N. J., & Williams, J. N. (2020). Evidence From High-Resolution Topography for Multiple Earthquakes on High Slip-to-Length Fault Scarps: The Bilila-Mtakataka Fault, Malawi. *Tectonics*, *39*(2), e2019TC005933. https://doi.org/10.1029/2019TC005933

Jackson, J., & Blenkinsop, T. (1997). The Bilila-Mtakataka fault in Malawi: an active, 100-km long, normal fault segment in thick seismogenic crust. *Tectonics*, *16*(1), 137–150. https://doi.org/10.1029/96TC02494

Kanamori, H., & Rivera, L. (2006). Energy Partitioning During an Earthquake. *Earthquakes: Radiated Energy and the Physics of Faulting*, *170*, 3–13. https://doi.org/10.1029/170GM03

Kelly, C. M., Faulkner, D. R., & Rietbrock, A. (2017). Seismically invisible fault zones: Laboratory insights into imaging faults in anisotropic rocks. *Geophysical Research Letters*, *44*(16), 8205–8212. https://doi.org/10.1002/2017GL073726

Kirkpatrick, J. D., Bezerra, F. H. R., Shipton, Z. K., Do Nascimento, A. F., Pytharouli, S. I., Lunn, R. J., & Soden, A. M. (2013). Scale-dependent influence of pre-existing basement shear zones on rift faulting: A case study from NE Brazil. *Journal of the Geological Society*, *170*(2), 237–247. https://doi.org/10.1144/jgs2012-043

Lacroix, B., Tesei, T., Oliot, E., Lahfid, A., & Collettini, C. (2015). Early weakening processes inside thrust fault. *Tectonics*. https://doi.org/10.1002/2014TC003716

Laõ-Dávila, D. A., Al-Salmi, H. S., Abdelsalam, M. G., & Atekwana, E. A. (2015). Hierarchical segmentation of the Malawi Rift: The influence of inherited lithospheric heterogeneity and kinematics in the evolution of continental rifts. *Tectonics*, *34*(12), 2399–2417. https://doi.org/10.1002/2015TC003953

Li, Y. G., De Pascale, G. P., Quigley, M. C., & Gravley, D. M. (2014). Fault damage zones of the M7.1 Darfield and M6.3 Christchurch earthquakes characterized by fault-zone trapped waves. *Tectonophysics*, *618*, 79–101. https://doi.org/10.1016/j.tecto.2014.01.029

Litchfield, N. J., Villamor, P., van Dissen, R. J., Nicol, A., Barnes, P. M., Barrell, D. J. A., et al. (2018). Surface rupture of multiple crustal faults in the 2016 Mw 7.8 Kaikōura, New Zealand, earthquake. *Bulletin of the Seismological Society of America*, *108*(3B), 1496–1520. https://doi.org/10.1785/0120170300

Lockner, D. A., Byerlee, J. D., Kuksenko, V., Ponomarev, A., & Sidorin, A. (1991). Quasi-static fault growth and shear fracture energy in granite. *Nature*, *350*(6313), 39–42.

https://doi.org/10.1038/350039a0

McBeck, J., Mair, K., & Renard, F. (2019). Linking macroscopic failure with micromechanical processes in layered rocks: How layer orientation and roughness control macroscopic behavior. *Tectonophysics*, *750*, 229–242. https://doi.org/10.1016/j.tecto.2018.11.016

McKay, L., Lunn, R. J., Shipton, Z. K., Pytharouli, S., & Roberts, J. J. (2021). Do intraplate and plate boundary fault systems evolve in a similar way with repeated slip events? *Earth and Planetary Science Letters*, *559*, 116757. https://doi.org/10.1016/j.epsl.2021.116757

Micklethwaite, S., & Cox, S. F. (2004). Fault-segment rupture, aftershock-zone fluid flow, and mineralization. *Geology*, *32*(9), 813–816.

Misra, S., Ellis, S., & Mandal, N. (2015). Fault damage zones in mechanically layered rocks: The effects of planar anisotropy. *Journal of Geophysical Research: Solid Earth*, *120*(8), 5432–5452. https://doi.org/10.1002/2014JB011780

Mitchell, T. M., & Faulkner, D. R. (2009). The nature and origin of off-fault damage surrounding strike-slip fault zones with a wide range of displacements: A field study from the Atacama fault system, northern Chile. *Journal of Structural Geology*, *31*(8), 802–816. https://doi.org/10.1016/j.jsg.2009.05.002

Paton, D. A. (2006). Influence of crustal heterogeneity on normal fault dimensions and evolution: southern South Africa extensional system. *Journal of Structural Geology*, *28*(5), 868–886. https://doi.org/10.1016/j.jsg.2006.01.006

Phillips, T. B., Jackson, C. A. L., Bell, R. E., Duffy, O. B., & Fossen, H. (2016). Reactivation of intrabasement structures during rifting: A case study from offshore southern Norway. *Journal of Structural Geology*, *91*, 54–73. https://doi.org/10.1016/j.jsg.2016.08.008

Renard, F., Weiss, J., Mathiesen, J., Ben-Zion, Y., Kandula, N., & Cordonnier, B. (2018).

Critical Evolution of Damage Toward System-Size Failure in Crystalline Rock. *Journal of Geophysical Research: Solid Earth*, *123*(2), 1969–1986. https://doi.org/10.1002/2017JB014964

Ring, U. (1994). The influence of preexisting structure on the evolution of the Cenozoic Malawi rift (East African rift system). *Tectonics*, *13*(2), 313–326. https://doi.org/10.1029/93TC03188

Rotevatn, A., Jackson, C. A. L., Tvedt, A. B. M., Bell, R. E., & Blækkan, I. (2019). How do normal faults grow? *Journal of Structural Geology*, *125*, 174–184. https://doi.org/10.1016/j.jsg.2018.08.005

Sagy, A., Brodsky, E. E., & Axen, G. J. (2007). Evolution of fault surface roughness with slip. *Geology*, *35*(3), 283–286. https://doi.org/10.1130/G23235A.1

Savage, H. M., & Brodsky, E. E. (2011). Collateral damage: Evolution with displacement of fracture distribution and secondary fault strands in fault damage zones. *Journal of Geophysical Research: Solid Earth*, *116*(3), B03405. https://doi.org/10.1029/2010JB007665

Scholz, C. A., Shillington, D. J., Wright, L. J. M., Accardo, N., Gaherty, J. B., & Chindandali, P. (2020). Intrarift fault fabric, segmentation, and basin evolution of the Lake Malawi (Nyasa) Rift, East Africa. *Geosphere*, *16*(5), 1293–1311. https://doi.org/10.1130/GES02228.1

Schwanghart, W., & Scherler, D. (2014). Short Communication: TopoToolbox 2 - MATLAB-based software for topographic analysis and modeling in Earth surface sciences. *Earth Surface Dynamics*, *2*(1), 1–7. https://doi.org/10.5194/esurf-2-1-2014

Shipton, Z. K., Evans, J. P., Abercrombie, R. E., & Brodsky, E. E. (2006). The missing sinks: Slip localization in faults, damage zones, and the seismic energy budget. *Geophysical Monograph Series*, *170*, 217–222. https://doi.org/10.1029/170GM22

Shipton, Z. K., Roberts, J., Comrie, E., Kremer, Y., Lunn, R., & Caine, J. (2019). Fault fictions: cognitive biases in the conceptualization of fault zones. *Geological Society Special Publications*.

Sibson, R. H. (1977). Fault rocks and fault mechanisms. *Journal of the Geological Society, 133*(3), 191–213. https://doi.org/10.1144/gsjgs.133.3.0191

Simpson, J., Adam, L., van Wijk, K., & Charoensawan, J. (2020). Constraining Microfractures in Foliated Alpine Fault Rocks With Laser Ultrasonics. *Geophysical Research Letters*, *47*(8). https://doi.org/10.1029/2020GL087378

Soden, A. M., Shipton, Z. K., Lunn, R. J., Pytharouli, S. I., Kirkpatrick, J. D., Do Nascimento, A. F., & Bezerra, F. H. R. (2014). Brittle structures focused on subtle crustal heterogeneities: Implications for flow in fractured rocks. *Journal of the Geological Society*, *171*(4), 509–524. https://doi.org/10.1144/jgs2013-051

Stevens, V. L., Sloan, R. A., Chindandali, P. R., Wedmore, L. N. J., Salomon, G. W., & Muir, R. A. (2021). The Entire Crust can be Seismogenic: Evidence from Southern Malawi. *Tectonics*, *40*(6), e2020TC006654. https://doi.org/10.1029/2020tc006654

Tinti, E., Spudich, P., & Cocco, M. (2005). Earthquake fracture energy inferred from kinematic rupture models on extended faults. *Journal of Geophysical Research: Solid Earth*, *110*(12), 1–25. https://doi.org/10.1029/2005JB003644

Torabi, A., & Berg, S. S. (2011). Scaling of fault attributes: A review. *Marine and Petroleum Geology*. https://doi.org/10.1016/j.marpetgeo.2011.04.003

Torabi, A., Ellingsen, T. S. S., Johannessen, M. U., Alaei, B., Rotevatn, A., & Chiarella, D. (2020). Fault zone architecture and its scaling laws: where does the damage zone start and stop? *Geological Society, London, Special Publications, 496*(1), 99–124. https://doi.org/10.1144/sp496-2018-151

Tulloch, A. J. (1979). Secondary Ca-Al silicates as low-grade alteration products of granitoid biotite. *Contributions to Mineralogy and Petrology*, *69*(2), 105–117. https://doi.org/10.1007/BF00371854

Vittori, E., Delvaux, D., & Kervyn, F. (1997). Kanda fault: A major seismogenic element west of the Rukwa Rift (Tanzania, East Africa). *Journal of Geodynamics*, *24*(1–4), 139–153. https://doi.org/10.1016/S0264-3707(96)00038-5

Walsh, J. J., Nicol, A., & Childs, C. (2002). An alternative model for the growth of faults. *Journal of Structural Geology*, *24*(11), 1669–1675. https://doi.org/10.1016/S0191-8141(01)00165-1

Walshaw, R. D. (1965). The Geology of the Nchue-Balaka Area. *Bulletin of the Geological Survey, Malawi*, *19*.

Wedmore, L. N. J., Williams, J. N., Biggs, J., Fagereng, Å., Mphepo, F., Dulanya, Z., et al. (2020). Structural inheritance and border fault reactivation during active early-stage rifting along the Thyolo fault, Malawi. *Journal of Structural Geology*, *139*, 104097. https://doi.org/10.1016/j.jsg.2020.104097

Wedmore, L. N. J., Biggs, J., Floyd, M., Fagereng, Å., Mdala, H., Chindandali, P. R. N., et al. (2021). Geodetic constraints on cratonic microplates and broad strain during rifting of thick Southern Africa lithosphere. *Geophysical Research Letters*.

Wheeler, W. H., & Karson, J. A. (1989). Structure and kinematics of the Livingstone Mountains border fault zone, Nyasa (Malawi) Rift, southwestern Tanzania. *Journal of African Earth Sciences*, *8*(2–4), 393–413. https://doi.org/10.1016/S0899-5362(89)80034-X

Williams, J. N., Toy, V. G., Massiot, C., McNamara, D. D., Smith, S. A. F., & Mills, S. (2018). Controls on fault zone structure and brittle fracturing in the foliated hanging wall of the Alpine Fault. *Solid Earth*, *9*(2), 469–489. https://doi.org/10.5194/se-9-469-2018

Williams, J. N., Fagereng, Å., Wedmore, L. N. J., Biggs, J., Mphepo, F., Dulanya, Z., et al. (2019). How Do Variably Striking Faults Reactivate During Rifting? Insights From Southern Malawi. *Geochemistry, Geophysics, Geosystems*, *20*(7), 3588–3607. https://doi.org/10.1029/2019GC008219

Wilson, B., Dewers, T., Reches, Z., & Brune, J. (2005). Particle size and energetics of gouge from earthquake rupture zones. *Nature*, *434*(7034), 749–752. https://doi.org/10.1038/nature03433

Woodcock, N. H., & Mort, K. (2008). Classification of fault breccias and related fault rocks. *Geological Magazine*, *145*(03), 435–440. https://doi.org/10.1017/S0016756808004883

Zangerl, C., Loew, S., & Eberhardt, E. (2006). Structure, geometry and formation of brittle discontinuities in anisotropic crystalline rocks of the central Gotthard massif, Switzerland. *Eclogae Geologicae Helvetiae*, *99*(2), 271–290. https://doi.org/10.1007/s00015-006-1190-0

List of Figures

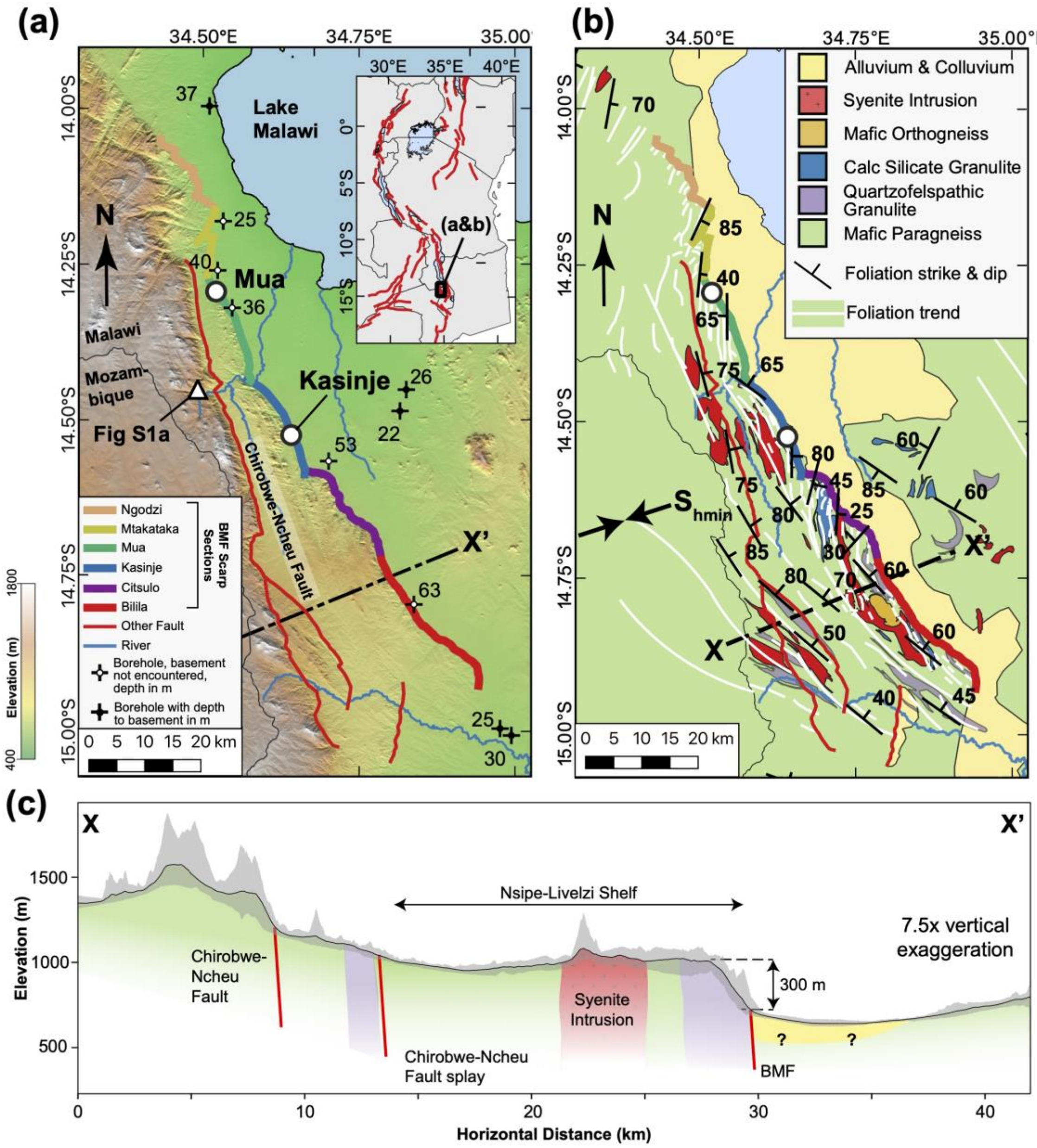

Figure 1: Geologic and geomorphic context of the Bilila-Mtakataka Fault (BMF). (a) The six sections of the BMF scarp [*Hodge et al.*, 2018] underlain by a 12 m resolution TanDEM-X digital elevation model, and (b) its surrounding geologic units and foliation orientations [*Dawson & Kirkpatrick*, 1968; *Hodge et al.*, 2018; *Walshaw*, 1965]. Inset in (a), the BMF location in the context of the East African Rift. Azimuth of minimum horizontal stress (S_{hmin}) from a focal mechanism stress inversion [*Williams et al.*, 2019]. (c) Regional scale cross section through the BMF at the point of its maximum footwall relief [*Jackson & Blenkinsop*,

1997], with key as in (b). Black line and shading represent mean and range of topography in a swath 2.5 km either side of the line shown in (a) [*Schwanghart & Scherler*, 2014].

Figure 2

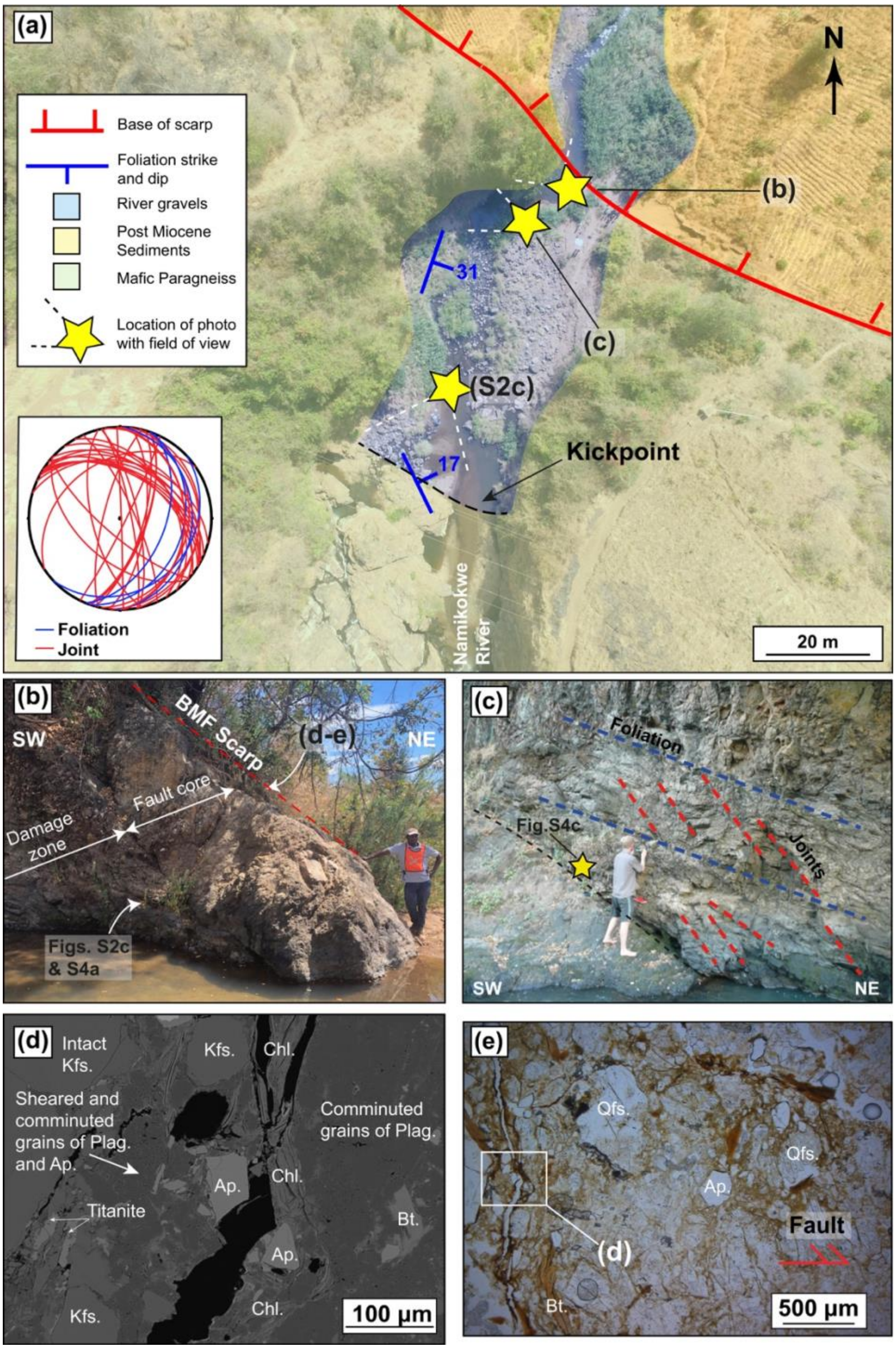

Figure 2: Field site at Mua with microstructural observations of BMF-related deformation. (a) Unmanned aerial vehicle (UAV) photograph underlain by geologic/geomorphic units with (inset) equal area stereonet depicting foliation and joint orientations. (b) Exposure adjacent to the BMF scarp, and (c) damage zone at Mua with <0.1 m spaced joints that are oblique to the

foliation. (d) Backscatter electron image of thin section from sample adjacent to the BMF scarp with comminuted plagioclase (Plag.) and chlorite (Chl.) grains surrounding K-feldspar (Kfs.) clasts. Mineral identification based on EDS map shown in Fig S3a. Bt.; Biotite, Ap.; Apatite. (e) Photomicrograph in plane polarised light (PPL) of area shown in (d). Qfs, Quartzofeldpathic porphyroclast.

Figure 3

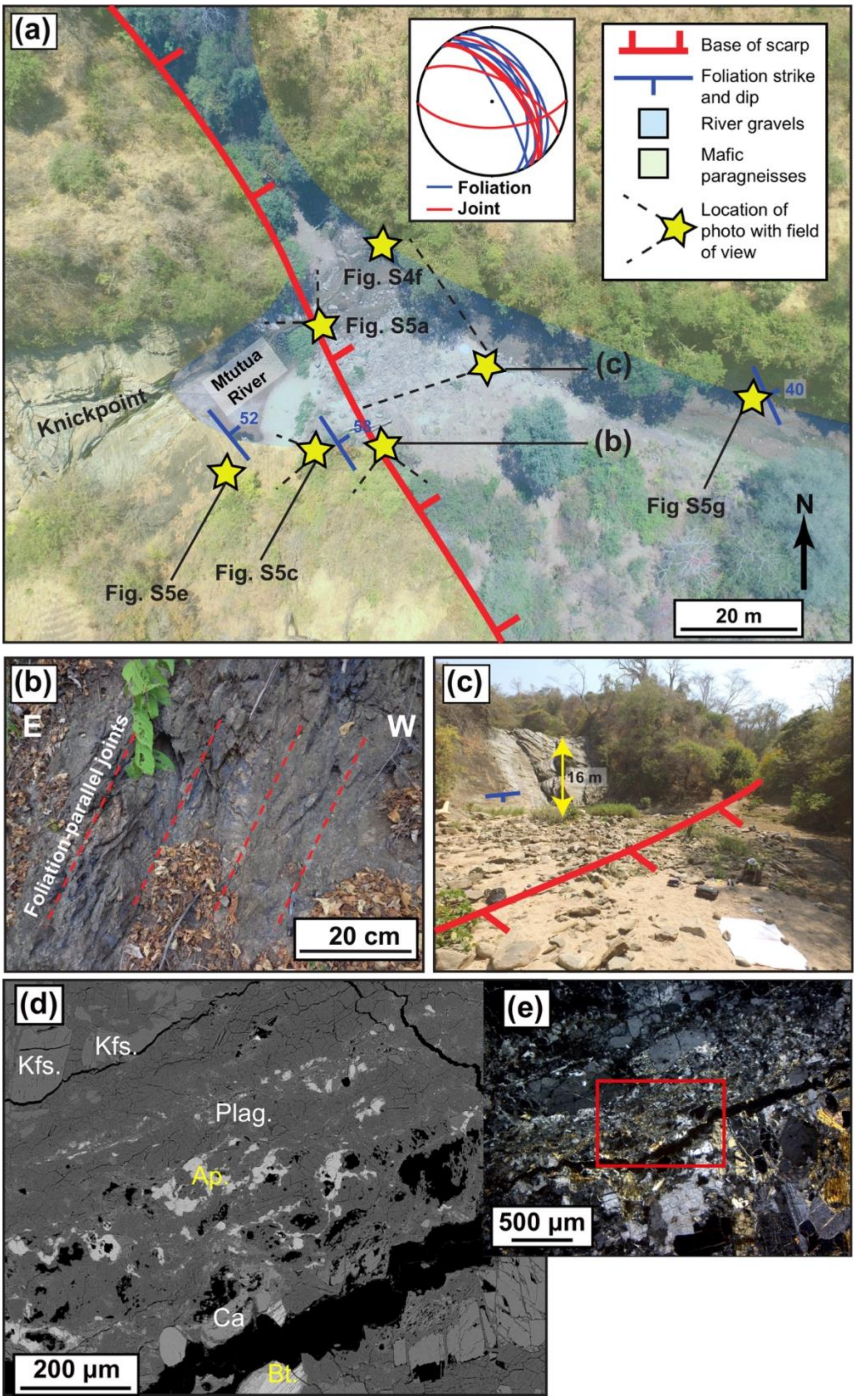

(a)
Foliation
Joint
Base of scarp
Foliation strike and dip
River gravels
Mafic paragneisses
Location of photo with field of view
Fig. S4f
Fig. S5a
Mtutua River
Knickpoint
52
58
40
(c)
(b)
Fig S5g
Fig. S5e
Fig. S5c
N
20 m
(b)
E
W
Foliation-parallel joints
20 cm
(c)
16 m
(d)
Kfs.
Kfs.
Plag.
Ap.
Ca
Bt.
200 µm
(e)
500 µm

Figure 3: Field site at Kasinje with microstructural observations of BMF-related deformation: (a) UAV image of site, (b) BMF damage zone exposure, and (c) oblique view of scarp and knickpoint. (d) Backscattered electron image of fragmented plagioclase (Plag.), calcite (Ca.), and apatite (Ap.) grains from sample adjacent to scarp. Kfs.; K-feldspar, Bt.; Biotite. (e) Photomicrograph of region shown in (d) taken in Cross Polarised Light (XPL).

Figure 4

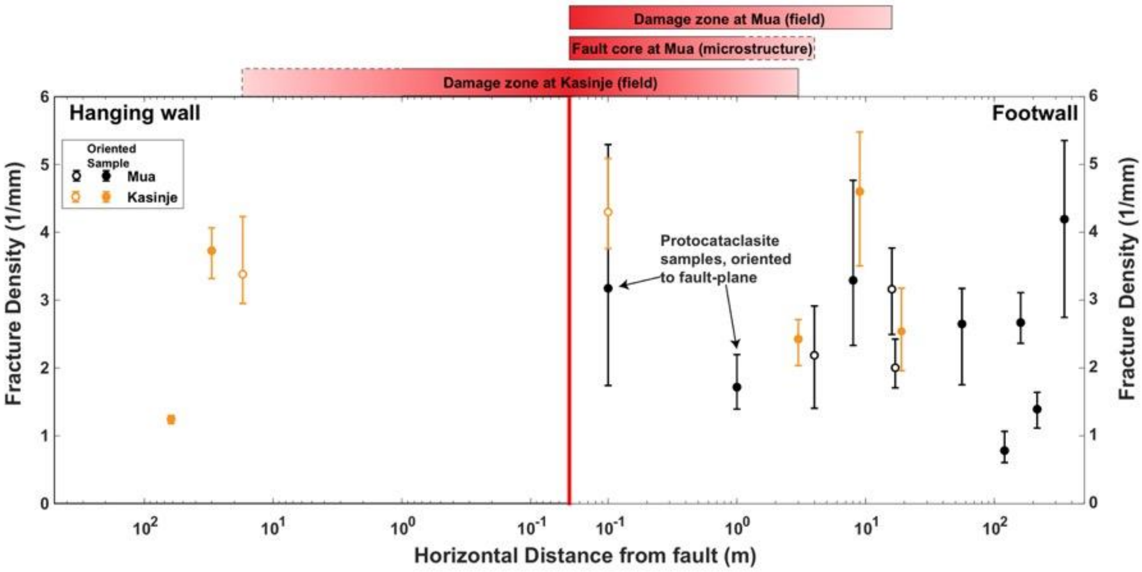

Figure 4: Area-weighted average microscale fracture density in quartz and feldspar grains plotted against horizontal distance from the BMF scarp. Error bars represent the fracture density range over the three sample areas analysed within each thin section. Extent of different fault zone structure components also shown for Mua and Kasinje; lines dashed for where interpretation is based on maximum extent of component due to limited sampling.

[Geophysical Research Letters]

Supporting Information for

Low dissipation of earthquake energy along faults that follow pre-existing weaknesses: field and microstructural observations of Malawi's Bilila-Mtakataka Fault

Jack N. Williams[a,b], Åke Fagereng[a], Luke N.J. Wedmore[b], Juliet Biggs[b], Hassan Mdala[c], Felix Mphepo[c], Michael Hodge[a]

[a]School of Earth and Environmental Sciences, Cardiff University, Cardiff, UK

[b]School of Earth Sciences, University of Bristol, Bristol, UK

[c]Geological Survey Department, Mzuzu Regional Office, Mzuzu, Malawi]

Contents of this file

Figures S1 to S5
Tables S1

Introduction

Figures S1-S5 provide additional context of the geomorphology around the Bilila-Mtakataka Fault, to our field observations, and microstructural analysis.

Table S1 lists the samples on which microstructural analysis was performed, their lithology, and their sampling locality.

Figure S1.

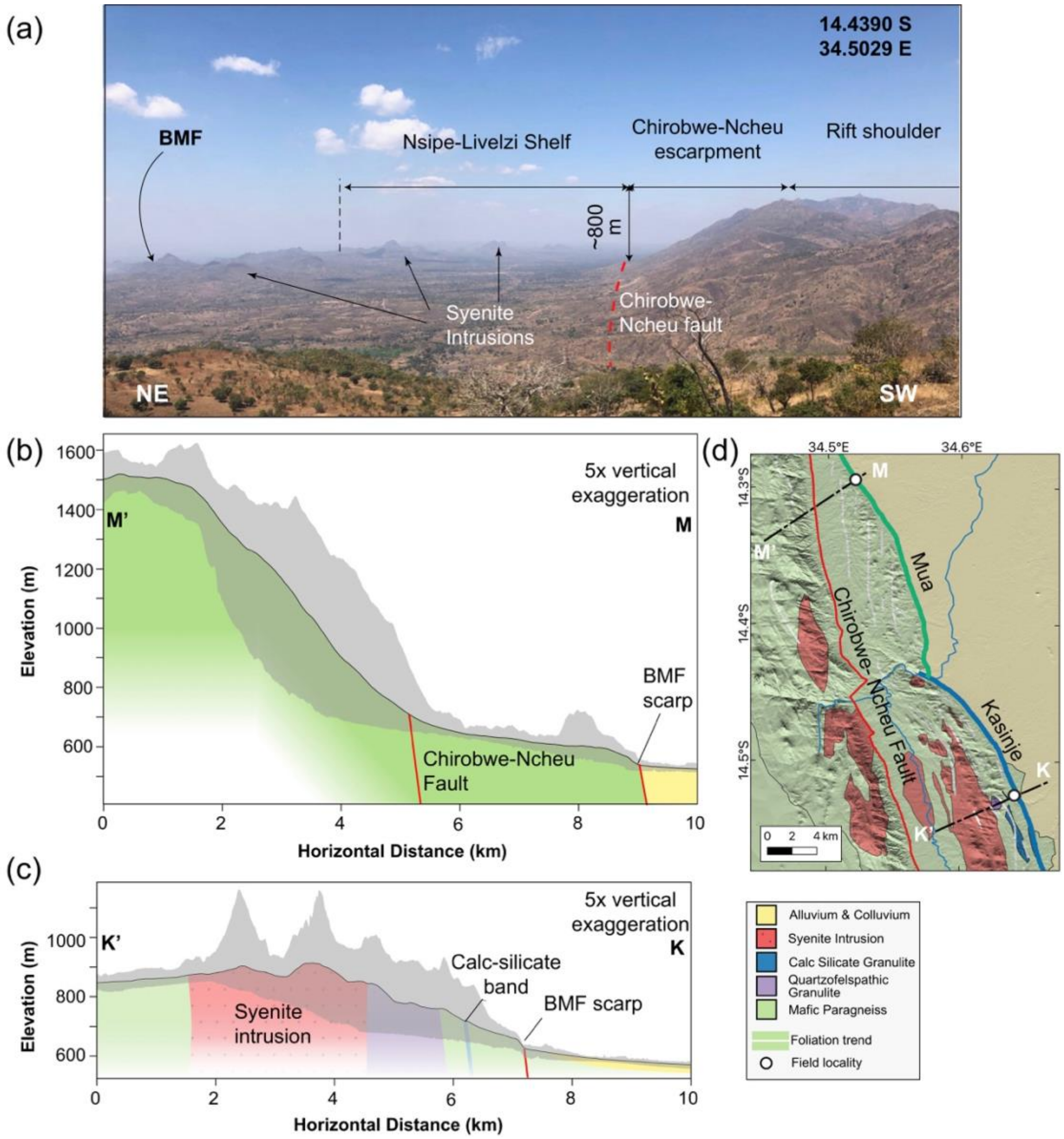

Figure S1: (a) Overview of the Bilila Mtakataka Fault's (BMF) footwall geomorphology taken from the Chirobwe-Ncheu Fault escarpment. See Fig. 1a for location. (b&c) cross sections through the BMF field localities at (b) Mua and (c) Kasinje. Black line and shading represent mean and range of topography in a swath 2.5 km either side of profiles in (d) [Schwanghart & Scherler, 2014]. (d) Map with extent of Mua and Kasinje segments of the BMF and context of cross sections in (b) and (c). Geological units from [Walshaw, 1965] and [Hodge et al., 2018], and are underlain by a TanDEM-X digital elevation model.

Figure S2

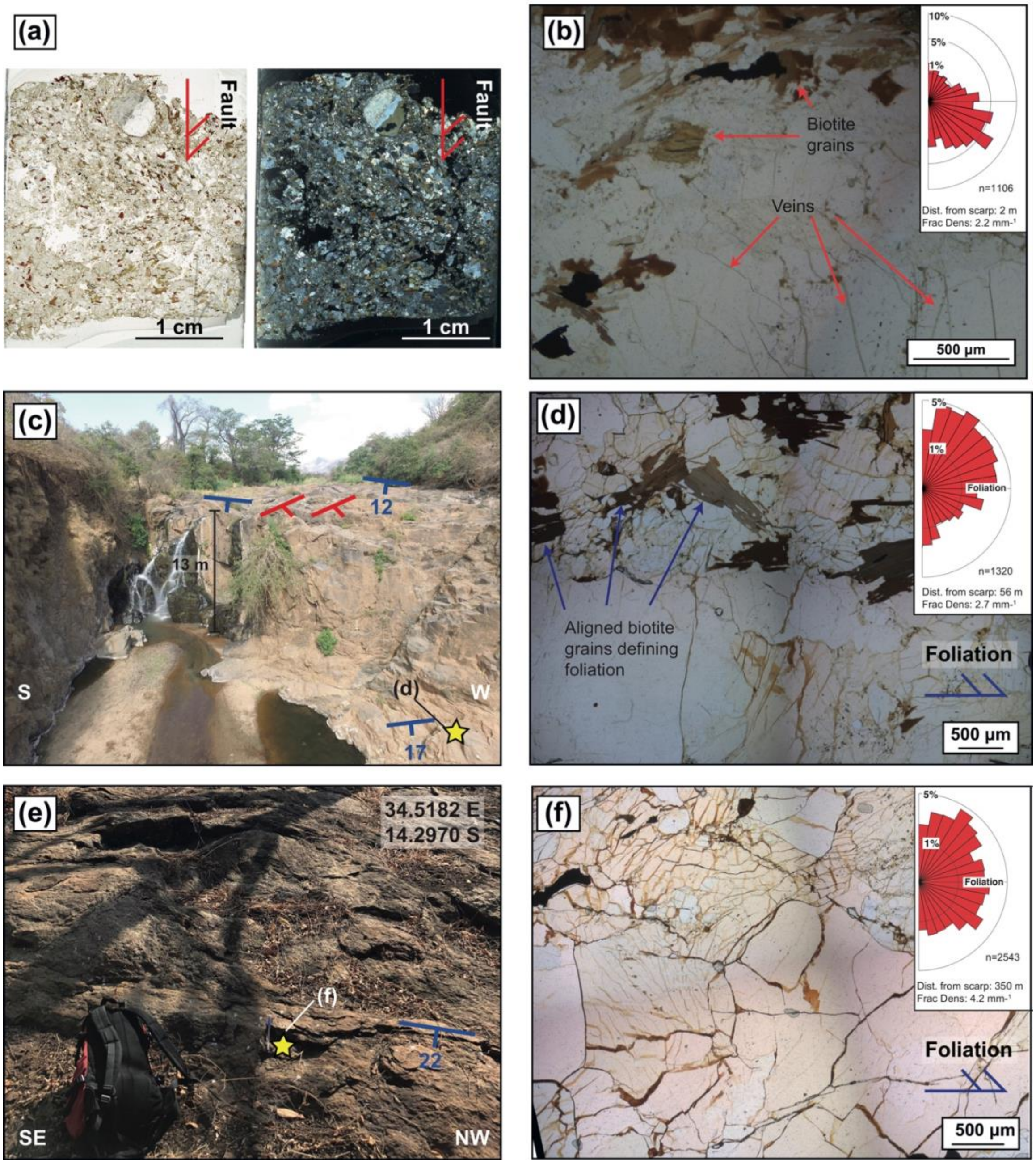

Figure S2: Field and photomicrographs from the BMF exposure at Mua. (a) Thin sections scan in plane polarised and cross polarised light (PPL and XPL respectively) of protocataclasite sample taken adjacent to exposed section of scarp at Mua. (b) Photomicrograph from the sample adjacent to the damage zone in PPL indicating foliation oblique veins in quartzofeldspathic grains. (c) Knickpoint at Mua, which is located beyond the damage zone where joints (blue strike and dip symbols) have >0.1 m spacing, dip moderately to the west, and cross cut the gently dipping foliation (red strike and dip symbols). (d) Photomicrograph in sample from near knickpoint where foliation oblique veins with fine grained brown fill are still prevalent. (e) Outcrop 350 m from the scarp at Mua where (f) a high density of veins is still observed in thin section. Inset in (c) and (d) are equal area rose plots of fracture segment orientations weighted by length [Healy et al., 2017]. Rose plots and reported fracture densities are for the three sample areas measured in each thin section.

Figure S3

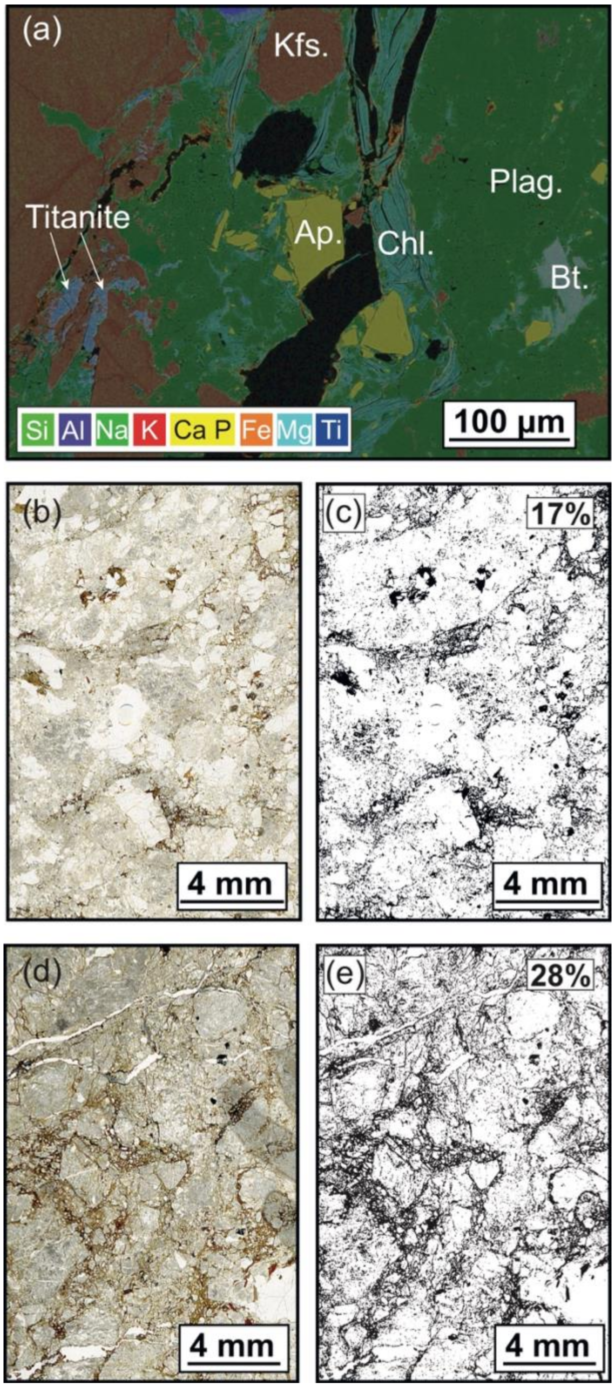

Figure S3: Analysis of matrix in BMF protocataclasites from Mua. (a) False color Energy Dispersive Spectroscopy (EDS) element map with underlain Backscatter Electron Image for area shown in Figure 2d in the main text, in thin section sampled from the Bilila-Mtakataka Fault scarp at Mua. Kfs.; K-feldspar, Plag.; Plagioclase feldspar, Bt.; Biotite, Chl.; Chlorite, Ap.; Apatite. (b) Thin section scan of protocataclasite 0.1 m from scarp. In (c), an image threshold has been applied to (b) using ImageJ, with the dark areas interpreted to represent cataclasite matrix. The proportion of the image interpreted as matrix using this method is given in the top right of (c). (d&e) Equivalent to (b&c), but for a sample 1 m from the scarp. Note these are upper limits of matrix area, as undeformed biotite grains will be interpreted as matrix.

Figure S4

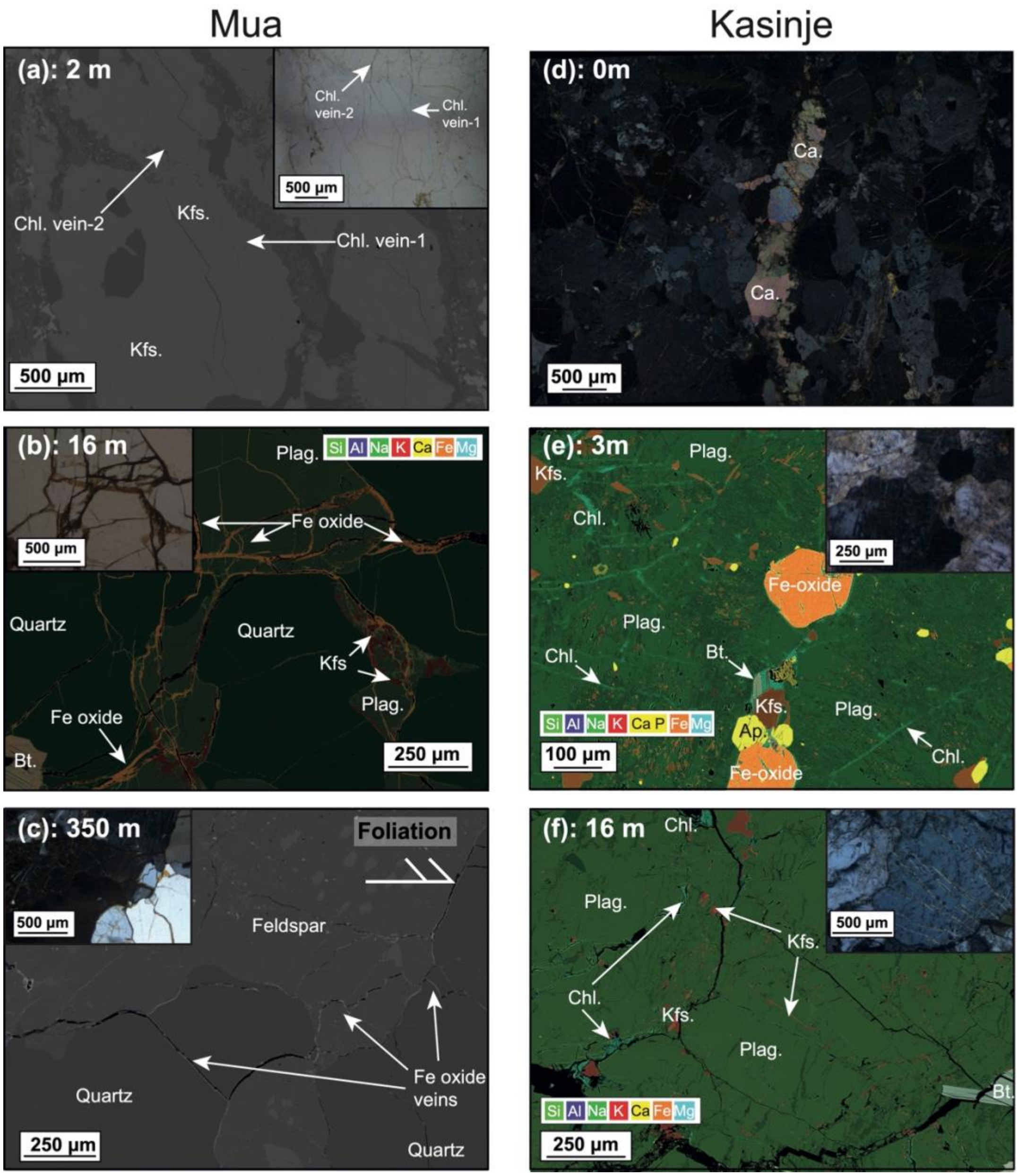

Figure S4: Representative images of microfracture networks around the BMF. Number next to label indicates horizontal distance thin section was sampled from the BMF scarp. Where applicable, insets show photomicrographs from a petrological microscope of the equivalent area in the SEM image. (a) Backscattered electron image (BSE) of chlorite veins in sample 2 m from BMF scarp at Mua (Fig. 2b) where grain-grain contacts are preserved. (b&c) Fe-oxide veins in thin sections from samples at greater distances from the BMF scarp at Mua. (b) is an Energy Dispersive Spectroscopy (EDS) element map underlain by BSE image and (c) is a BSE image. (d) Calcite veins adjacent to the BMF scarp at Kasinje in photomicrograph taken in XPL. (e&f) EDS element maps underlain by BSE image highlighting chlorite veins in samples of (e) footwall and (f) hanging wall country rock at Kasinje. Interpretation of vein fills in (a) and (c) from EDS point spectra. Kfs.; K-feldspar, Plag.; Plagioclase feldspar, Bt.; Biotite, Chl.; Chlorite, Ca.; Calcite, Ap.; Apatite.

Figure S5

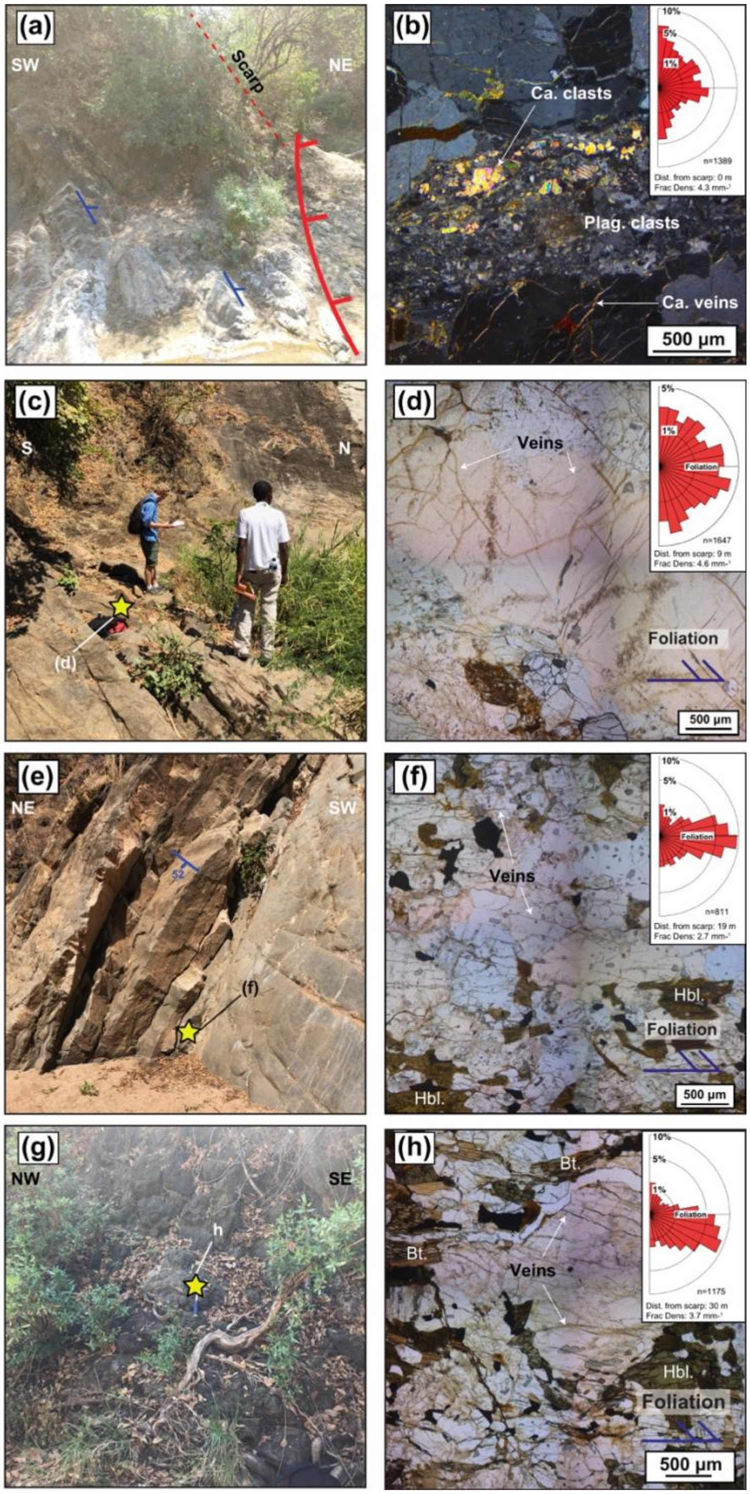

Figure S5: Field and micrographs of BMF exposure at Kasinje. For context of figures localities, see Fig. 3a in the main text. (a) Exposure adjacent to the BMF scarp with closely spaced foliation parallel joints. (b) Sample adjacent to scarp with fragmented calcite and plagioclase clasts taken in XPL. (c) Footwall exposure adjacent to the BMF damage zone at Kasinje show location of (d), photomicrograph taken in PPL of oblique veins with fine-grained brown fill in weakly foliated migmatic gneiss. (e) Exposure at base of Kasinje knickpoint with foliation parallel joints. Also shown is location of thin section in (f) where veins are aligned to the foliation. (g) Exposure in hanging wall of the BMF showing context of (h) with foliation parallel veins. Reported fracture densities and rose plots in (d), (f), and (h) are for fracture segment orientations weighted by length as in Figs S2.

Table S1. Samples used in microfracture density and Scanning Electron Microscope (SEM) analysis

Sample	Distance from BMF scarp (m)*	Longitude (E)	Latitude (S)	Lithology	Fracture density (mm^{-1})†	SEM analysis
<u>Mua</u>						
MBMF19-03	0.1	34.5204	14.2941	Protocataclasite	$3.2^{+2.1}_{-1.4}$	EDS point spectra & mapping
MBMF18-02	1	34.5204	14.2941	Protocataclasite	$1.7^{+0.5}_{-0.3}$	
MBMF18-03	2	34.5204	14.2941	Biotite gneiss	$2.2^{+0.7}_{-0.8}$	EDS point spectra
MBMF18-04	8	34.5204	14.2941	Biotite gneiss	$3.3^{+1.5}_{-1.0}$	
MBMF18-05	16	34.5204	14.2941	Biotite gneiss	$3.2^{+0.6}_{-0.7}$	EDS point spectra & mapping
BMF1-2	17	34.5204	14.2941	Biotite gneiss	$2.0^{+0.4}_{-0.3}$	
MBMF18-06	56	34.5199	14.2946	Biotite gneiss	$2.7^{+0.5}_{-0.9}$	
MBMF18-07	120	34.5195	14.2950	Biotite gneiss	$0.8^{+0.3}_{-0.2}$	
MBMF19-01	160	34.5193	14.2950	Biotite gneiss	$2.7^{+0.4}_{-0.3}$	
MBMF19-02	215	34.5188	14.2952	Biotite gneiss	$1.4^{+0.3}_{-0.3}$	
MBMF18-08	350	34.5182	14.2970	Biotite gneiss	$4.2^{+1.2}_{-1.4}$	EDS point spectra
<u>Kasinje</u>						
BMF4-4	0.1	34.6410	14.5244	Altered gneiss	$4.3^{+0.8}_{-0.5}$	EDS point spectra
K18-04	3	34.6410	14.5244	Migmatic gneiss	$2.4^{+0.3}_{-0.4}$	EDS point spectra & mapping
K18-03	9	34.6410	14.5244	Migmatic gneiss	$4.6^{+1.1}_{-0.9}$	
K18-06	16	34.6410	14.5244	Altered gneiss	$3.4^{+0.9}_{-0.4}$	EDS point spectra & mapping
K18-01	19	34.6408	14.5245	Hornblende-biotite gneiss	$2.7^{+0.6}_{-0.6}$	
K18-07	30	34.6413	14.5244	Quartzofeldspathic gneiss	$3.7^{+0.4}_{-0.3}$	
K18-08	62	34.6418	14.5250	Hornblende-biotite gneiss	$1.2^{+0.1}_{-0.1}$	

Note. *Measured as distance between sample and fault scarp along a horizontal line perpendicular to fault scarp. Distances <10 m, measured in field with tape measure, distances >10 m measured based on handheld GPS locations with an accuracy of 3-5 m. †Area-weighted average microfracture density for the three sample areas measured within each sample [*Wedmore et al.*, 2020]. Plus and minus values represent range of fracture densities over the three sample areas.